Multifilamentation of powerful optical pulses in silica

L. Bergé,[1] S. Mauger,[1] and S. Skupin[2,3]
[1]*CEA-DAM, DIF, F-91297 Arpajon, France*
[2]*Max-Planck-Institute for the Physics of Complex Systems, D-01187 Dresden, Germany*
[3]*Friedrich-Schiller-University, Institute of Condensed Matter Theory and Solid State Optics, D-07743 Jena, Germany*
(Received 22 October 2009; published 25 January 2010)

The multiple filamentation of powerful light pulses in fused silica is numerically investigated for central wavelengths at 355 nm and 1550 nm. We consider different values for beam waist and pulse duration and compare the numerical results with behaviors expected from the plane-wave modulational instability theory. Before the nonlinear focus, the spatiotemporal intensity patterns can be explained in the framework of this theory. Once the clamping intensity is reached, for long input pulse durations (∼1 ps), the ionization front defocuses all trailing components within a collective dynamic, and a spatial replenishment scenario takes place upon further propagation. Short pulses (∼50 fs) undergo similar ionization fronts, before an optically turbulent regime sets in. We observe moderate changes in the total temporal extent of ultraviolet pulses and in the corresponding spectra. In contrast, infrared pulses may undergo strong temporal compression and important spectral broadening. For short input pulses, anomalous dispersion and self-steepening push all pulse components to the trailing edge, where many small-scaled filaments are nucleated. In the leading part of the pulse, different spatial landscapes, e.g., broad ring patterns, may survive and follow their own propagation dynamics.

DOI: 10.1103/PhysRevA.81.013817 PACS number(s): 42.65.Tg, 52.38.Hb, 42.68.Ay

I. INTRODUCTION

High-power femtosecond laser sources can nowadays generate light filaments propagating over long distances in transparent media, such as air, noble gases, liquids, and glasses. The basic phenomena sustaining the filamentation dynamics are the optical Kerr self-focusing developing along the earliest propagation stages, followed by plasma generation that defocuses the most intense components of the pulse. Fundamental aspects and applications of this process have been reviewed in several articles [1–5]. Powerful beams with peak powers above the critical power for self-focusing transform laser radiation into a narrow light "rod" clamped with a plasma channel, capable of running over several Rayleigh lengths along the optical path. With ultrashort pulses, this filamentation mechanism is generally accompanied by supercontinuum generation and production of sharp peaks in the temporal pulse profile, some of them can be isolated and exploited in efficient self-compression setups [6–8].

Besides their ability to collapse and self-compress, femtosecond pulses with high enough intensity can also become modulationally unstable and decay into multiple filaments under the action of the local ambient noise [9–11]. The consequence is rather catastrophic, in the sense that this "multifilamentation" breaks the homogeneity of the laser focal spot through the random nucleation of filaments. Limitations of this harmful phenomenon in air have been proposed by, e.g., playing on beam ellipticity [12] or by introducing either periodic meshes or masks [13,14] in the beam profile. However, rendering multifilamentation more deterministic is not acquired for beams conveying several thousands of critical powers over long paths, in particular in condensed materials involving high nonlinear Kerr indices and strong chromatic dispersion. Understanding the creation of multiple filaments in such media is thus prerequisite to their future control.

Several works have been devoted to the filamentation of femtosecond pulses in dielectrics, such as fused silica. Using laser sources operating at the wavelength of 800 nm, pioneering investigations revealed that ∼10–40 μm-waisted filaments with input energy of 2 μJ could travel upon 1 cm of silica in loosely focused geometry [15]. Tightly focused radiation, in contrast, produced a breakdown plasma with an electron density up to 10^{20} cm^{-3} resulting in the formation of a diffusion damage region [16]. More recently, measurements of plasma channels created from 248 nm, 450 fs pulses reported an electron density of 4×10^{19} cm^{-3}, contributing by an index change of 0.4×10^{-3} after irradiation by one pulse [17]. Filamentation in glasses allows photoinduced micromodifications of optical materials without thermal damage at moderate fluences <0.1 J/cm^2 [18]. At 800 nm, irreversible modification lines occur when the refraction index change attains 5×10^{-3}. In the near-infrared domain (1558 nm), structural modifications supported by a refraction index change of about 1.2×10^{-3} driven by 870 fs pulses were also observed in optically-fabricated gratings [19].

The above investigations, however, were mostly limited to propagation regimes along which the pulse preserved its spatial integrity. To the best of our knowledge, nothing is known about pulses triggering multiple filamentation in dense materials. One reason for this lack of knowledge may simply be the size of the corresponding computer simulation. Letting, e.g., mm-broad beams break up into multiple cells in the diffraction plane indeed requires to reach ∼1 μm spatial resolution in such media. Concerning long pulses with, e.g., ∼1 ps full-width at half-maximum (FWHM) durations, the temporal resolution must be below the fs scale, in order to correctly resolve the plasma response. These constraints can nowadays be fulfilled with the advent of massively-parallel clusters. Using the novel computer machine Titane of the Commissariat for Atomic Energy (CEA), we have investigated the nonlinear behaviors of pulses operating at the ultraviolet (UV) wavelength of 355 nm, leading to normal group-velocity dispersion, and others operating in the infrared (IR) at 1550 nm, leading to anomalous group-velocity dispersion.

In the following, we assume a linearly-polarized electric field $\sim\mathcal{E}e^{ik_0z-i\omega_0t}+$ c.c., with the envelope $\mathcal{E}(x,y,z,t)$ normalized such that the pulse intensity is $I=|\mathcal{E}|^2$. The field envelope is coupled to the free electron density $\rho(x,y,z,t)$ created by photo-ionization, through an extended nonlinear Schrödinger equation [3]

$$\partial_z\mathcal{E}=\frac{i}{2k_0}T^{-1}\nabla_\perp^2\mathcal{E}+i\mathcal{D}\mathcal{E}-i\frac{k_0}{2n_0^2\rho_c}T^{-1}\rho\mathcal{E}-\frac{\sigma}{2}\rho\mathcal{E}-\frac{U_iW(I)(\rho_{\rm nt}-\rho)}{2I}\mathcal{E}+i\frac{\omega_0}{c}n_2T\int\mathcal{R}(t-t')|\mathcal{E}(t')|^2dt'\mathcal{E},\quad(1)$$

$$\mathcal{R}(t)=(1-g)\delta(t)+g\theta(t)\frac{1+\omega_R^2\tau_R^2}{\omega_R\tau_R^2}e^{-t/\tau_R}\sin(\omega_Rt),\quad(2)$$

$$\partial_t\rho=W(I)(\rho_{\rm nt}-\rho)+\sigma\rho I/U_i-\rho/\tau_{\rm rec},\quad(3)$$

where z is the propagation variable, $\nabla_\perp^2=\partial_x^2+\partial_y^2$ the diffraction operator, and t the retarded time of the pulse in a frame moving at group velocity. The wave number $k_0=n_0\omega_0/c$ involves the linear refractive index $n_0=n(\omega_0)$ at central frequency ω_0. The operator $\mathcal{D}=\sum_{n\geqslant2}(k^{(n)}/n!)(i\partial_t)^n$ accounts for dispersion formally involving the derivatives $k^{(n)}\equiv\partial^nk/\partial\omega^n|_{\omega_0}$. It includes the coefficients $k^{(2)}\equiv k''$ for group-velocity dispersion (GVD) and $k^{(3)}\equiv k'''$ for third-order dispersion (TOD). Values for glass dispersion are taken from Ref. [20]. The operator $T=1+(i/\omega_0)\partial_t$ corrects the slowly-varying envelope approximation and is responsible for space-time focusing and self-steepening [21]. n_2 denotes the nonlinear Kerr index and $\rho_c\simeq1.11\times10^{21}/\lambda_0^2[\mu{\rm m}]\ {\rm cm}^{-3}$ is the critical plasma density. The nonlinear Kerr response includes a Raman-delayed contribution with ratio g varying with the laser wavelength [20,22]. The Keldysh rate for crystals is employed to model ionization in glass [23], using a reduced (electron-hole) mass of silica equal to 0.635 and considering the ionization potential $U_i=7.8$ eV. The initial density of SiO_2 molecules is $\rho_{\rm nt}=2.1\times10^{22}\ {\rm cm}^{-3}$ and the electron recombination time is set to $\tau_{\rm rec}=150$ fs. Besides dispersion coefficients and the constituents of the overall Kerr response Eq. (2), other physical parameters such as the avalanche cross sections σ have been recalled in Table I.

The propagation Eqs. (1) to (3) are integrated numerically for collimated pulses modeled at $z=0$ by an elongated, second-order supergaussian profile

$$\mathcal{E}(x,y,z=0,t)=\sqrt{I_0}e^{-\frac{x^4}{w_0^4}-\frac{4y^4}{w_0^4}}e^{-\frac{t^{2N}}{t_p^{2N}}},\quad(4)$$

where $I_0=2\pi P_{\rm in}/[P_{\rm cr}\Gamma^2(5/4)]$. Here, $P_{\rm in}$ is the input power, $P_{\rm cr}\simeq\lambda_0^2/2\pi n_0n_2$ denotes the critical power for self-focusing and $\Gamma(x)$ is the usual Euler gamma function. The input pulse (4) has the beam waist w_0 and the $1/e^2$ pulse half-width t_p. The exponent $N=1$ is used for modeling Gaussian pulses with short durations, $t_p=50$ fs (FWHM duration of about 60 fs), and millimeter spatial extents. The same exponent will take the value $N=2$, when we simulate long pulses with $t_p=500$ fs (FWHM duration of 1 ps) for smaller spatial beams.

Numerical simulations have been performed in full 3D geometry. The ratio of input power over critical has been chosen in such a way that the initial intensity I_0 lies inside a narrow range of values, namely $0.06\leqslant I_0\leqslant0.8\ {\rm TW/cm^2}$, corresponding to the wide power interval $P_{\rm in}/P_{\rm cr}=10$–$20\,000$ for various beam waists. For long pulses ($t_p=500$ fs), the spatial waist is small ($w_0=0.2$ mm), in order to concentrate on temporal distortions while keeping high resolution level. In this situation, we introduce a 5% random noise both into the spatial and temporal amplitudes of the initial beam. For short pulses ($t_p=50$ fs), the beams exhibit a broader waist ($w_0=1$ mm), in order to trigger full optical turbulence from a 5% random noise introduced into the beam spatial amplitude only. Simulations used resolutions of ~1 μm in (x,y) and ~0.5 fs in time for an adaptive step size along z, and ran over 1024 processors.

The paper is organized as follows. Section II adapts the modulational instability theory for plane waves to a nonlinear Schrödinger model including TOD, space-time focusing, and self-steepening, applied to the early self-focusing stage of propagation before plasma generation. Sections III and IV detail long and short pulse dynamics in the ultraviolet and near-infrared wavelength domains, respectively. Section V discusses the corresponding spectra while Sec. VI concludes the present work.

TABLE I. Physical parameters for silica at 355 nm and 1550 nm. Kerr indices are taken from Refs. [20,24].

Glass parameters vs. λ_0	355 nm	1550 nm
k'' (fs^2/cm)	1169	−279
k''' (fs^2/cm)	348	1510
n_0	1.47	1.44
n_2 (10^{-16} cm^2/W)	3.6	2.2
$P_{\rm cr}$ (MW)	0.37	12
g	0.15	0.18
τ_R (fs)	50	32
ω_R^{-1} (fs)	11.9	12.3
σ (10^{-19} cm^2)	1.108	21.56

II. MODULATIONAL INSTABILITY FOR PLANE WAVES

The most intense central part of the extended beams defined by Eq. (4) can be assimilated to plane waves destabilized by the action of random noise from $z=0$ until the self-focus point z_c, from which plasma generation occurs. Locally, the plane wave suffers oscillatory perturbations that grow with the exponential rate Γ as

$$\mathcal{E}\simeq\{\sqrt{I_0}+[\tilde{a}(x,y,t)+i\tilde{b}(x,y,t)]e^{\Gamma z}\}e^{i\theta z},\quad(5)$$

where $\theta=(\omega_0n_2/c)I_0$, $\tilde{a},\tilde{b}$ are real-valued functions and $|\tilde{a}|,|\tilde{b}|\ll\sqrt{I_0}$. Discarding any plasma term together with the Raman-delayed contribution limited to only 18% of the overall Kerr nonlinearity, we plug Eq. (5) into

$$\partial_z\mathcal{E}=\frac{i}{2k_0}T^{-1}\nabla_\perp^2\mathcal{E}+i\mathcal{D}\mathcal{E}+\frac{i\omega_0n_2}{c}T|\mathcal{E}|^2\mathcal{E},\quad(6)$$

which can then be linearized straightforwardly. Performing the Fourier transform in time on the resulting equations by means of $[a(\overline{\omega}),b(\overline{\omega})]\equiv\int_{-\infty}^{+\infty}[\tilde{a}(t),\tilde{b}(t)]e^{i\overline{\omega}t}dt$ [25], we obtain the

following spectral problem:

$$\Gamma b = \left[\frac{\nabla_\perp^2}{2k_0\left(1+\frac{\overline{\omega}}{\omega_0}\right)} + \sum_{n\geqslant 2} \frac{k^{(n)}}{n!}\overline{\omega}^n + \frac{2\omega_0 n_2}{c}\left(1+\frac{3\overline{\omega}}{2\omega_0}\right) I_0 \right] a, \tag{7}$$

$$\Gamma a = \left[-\frac{\nabla_\perp^2}{2k_0\left(1+\frac{\overline{\omega}}{\omega_0}\right)} - \sum_{n\geqslant 2} \frac{k^{(n)}}{n!}\overline{\omega}^n - \frac{n_2\overline{\omega}}{c} I_0 \right] b. \tag{8}$$

Under the hypothesis that a, b can be approximated by oscillatory functions $a, b \sim \cos(\vec{k}_\perp \cdot \vec{r})$ with spatial wave number $k_\perp = \sqrt{k_x^2 + k_y^2}$, the perturbation growth rate follows from the positive real root of

$$\Gamma^2 = \left[\frac{2\omega_0 n_2}{c}\left(1+\frac{3\overline{\omega}}{2\omega_0}\right) I_0 + \sum_{n\geqslant 2} \frac{k^{(n)}}{n!}\overline{\omega}^n - \frac{k_\perp^2}{2k_0\left(1+\frac{\overline{\omega}}{\omega_0}\right)} \right] \times \left[\frac{k_\perp^2}{2k_0\left(1+\frac{\overline{\omega}}{\omega_0}\right)} - \sum_{n\geqslant 2} \frac{k^{(n)}}{n!}\overline{\omega}^n - \frac{n_2\overline{\omega}}{c} I_0 \right]. \tag{9}$$

The previous formula generalizes that earlier derived by Litvak *et al.* in [26] to higher-order dispersion, space-time focusing, and self-steepening. Following [25], the Fourier frequency $\overline{\omega}$ corresponds to characteristic periodic fluctuations of the field envelope in time. In the diffraction plane, perturbative modes have the typical wave number $\sim k_\perp$, assuming isotropy of all light cells created by modulational instability (MI).

Below, we will limit high-order dispersion to TOD. By plotting Eq. (9), it can be checked that the T, T^{-1} operators describing pulse steepening downshift the instability branches by ~ 0.1 fs^{-1} only in the large frequency regions. So, space-time focusing and self-steepening do not deeply modify the zones of maximum instability in the $(k_\perp, \overline{\omega})$ plane. Keeping this property in mind, the maximum growth rate $\Gamma_{\max} \simeq \omega_0 n_2 I_0/c$ is reached by wave numbers and frequencies lying on the curves $k_\perp^2/2k_0 - \sum_{n=2,3}(k^{(n)}/n!)\overline{\omega}^n \simeq (\omega_0 n_2/c) I_0$. For uniform perturbations along time ($\overline{\omega} \to 0$), the instability is identical to Bespalov-Talanov's pioneering result [9] and is characterized by the optimum wave number $k_\perp^{\max} = \omega_0 n_2 I_0/c$. Perturbations uniform in the transverse plane ($k_\perp \to 0$) cannot grow when GVD is normal and prevails over higher-order dispersion.

In regimes of normal dispersion ($k'' > 0$) with relatively small TOD ($\lambda_0 = 355$ nm), the instability regions design hyperbolas, as shown by Figs. 1(a) and 1(b) for the intensity values $I_0 = 0.06$ and 0.46 TW/cm^2, respectively. In that case the action of TOD on modulational instability is negligible. In regimes of anomalous dispersion ($k'' < 0$) with relatively large TOD ($\lambda_0 = 1550$ nm), two instability regions occur, i.e., hyperbolas at large frequencies and ellipses at small frequencies. Examples are given in Figs. 1(c) and 1(d) for the intensity values $I_0 = 0.2$ and 0.73 TW/cm^2, respectively. In the latter case, we can see the hyperbolic branch associated with TOD merging with the elliptic branch when the input intensity takes high enough values.

As seen from Fig. 1(a), 355 nm pulses with moderate input intensity have the maximum perturbation wave number $k_\perp^{\max} \simeq 1378$ cm^{-1} yielding the optimum modulation wavelength

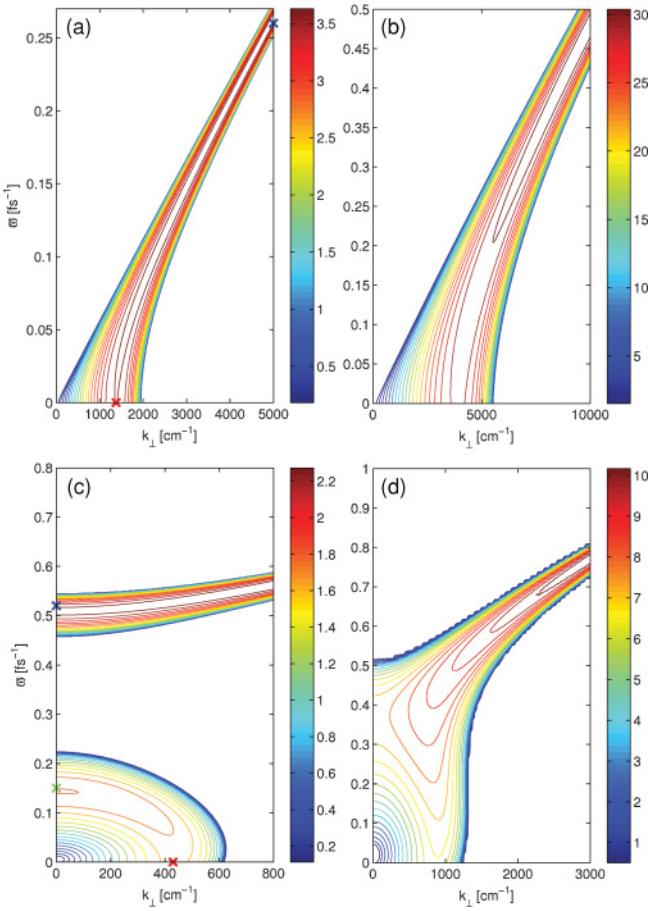

FIG. 1. (Color online) Contour plots of the growth rate Γ [cm^{-1}] in the plane $(k_\perp, \overline{\omega})$ for $\lambda_0 = 355$ nm: (a) $I_0 = 0.06$ TW/cm^2, (b) $I_0 = 0.46$ TW/cm^2; for $\lambda_0 = 1550$ nm: (c) $I_0 = 0.2$ TW/cm^2, (d) $I_0 = 0.73$ TW/cm^2. The colored crosses indicate positions of the variables $k_\perp$ and $\overline{\omega}$ used in Fig. 2.

$\lambda_{\text{opt}} = 2\pi/k_\perp^{\max} \approx 46$ μm in the limit $\overline{\omega} \to 0$. In the present case, Fig. 1(a) predicts occurrence of spatial modulations around $k_\perp \sim k_\perp^{\max}$. In Fig. 1(b), a higher input intensity causes a more severe instability, with $k_\perp^{\max} \simeq 3900$ cm^{-1} yielding 16 μm optimum modulations. With dominant GVD, there is no amplified unstable frequency in the limit $k_\perp \to 0$.

In contrast, 1550 nm pulses are characterized by two instability regions, in which anomalous dispersion may amplify modulations in time. In Fig. 1(c) we can indeed identify an elliptic region, dominated by GVD, reaching a maximum growth rate for $k_\perp \approx k_\perp^{\max} \simeq 430\,\text{cm}^{-1}$($\lambda_{\text{opt}} \sim 144$ μm) in the limit $\overline{\omega} \to 0$ and $\overline{\omega}_{\max} \approx 0.15$ fs^{-1}($\tau_{\text{opt}} \sim 42$ fs) in the limit of zero wave numbers. Above the elliptic zone, the hyperbolic branch, dominated by TOD, starts from higher frequencies $\overline{\omega}_{\max} \sim 0.52$ fs^{-1}($\tau_{\text{opt}} \sim 12$ fs). Destabilization of the pulse should thus proceed from these modulation scales. Figure 1(d) shows the instability domain of 1550 nm pulses with higher intensity. The hyperbolic (TOD) branch enters the GVD elliptic region at high frequencies. Both zones merge around the point of coordinates $k_\perp \approx k_\perp^{\max} = 875$ cm^{-1}, responsible for ~ 72 μm spatial modulations, and $\overline{\omega}_{\max} \simeq 0.35$ fs^{-1}, leading to ~ 18 fs temporal fluctuations.

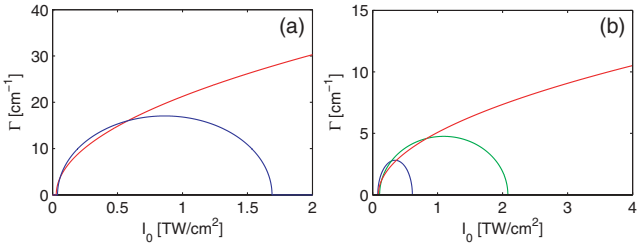

FIG. 2. (Color online) Growth rate Γ versus intensity I_0 for fixed points in the $(k_\perp, \overline{\omega})$ plane. (a) 355 nm: $k_\perp = 5000$ cm^{-1}, $\overline{\omega} = 0.26$ fs^{-1} (blue, lower line), and $k_\perp = 1378$ cm^{-1}, $\overline{\omega} = 0$ (red, upper line). (b) 1550 nm: $k_\perp = 0$, $\overline{\omega} = 0.52$ fs^{-1} (blue, lower line), $k_\perp = 0$, $\overline{\omega} = 0.15$ fs^{-1} (green, center line), and $k_\perp = 430$ cm^{-1}, $\overline{\omega} = 0$ (red, upper line). The respective positions of $k_\perp$ and $\overline{\omega}$ are marked in Fig. 1 by colored crosses.

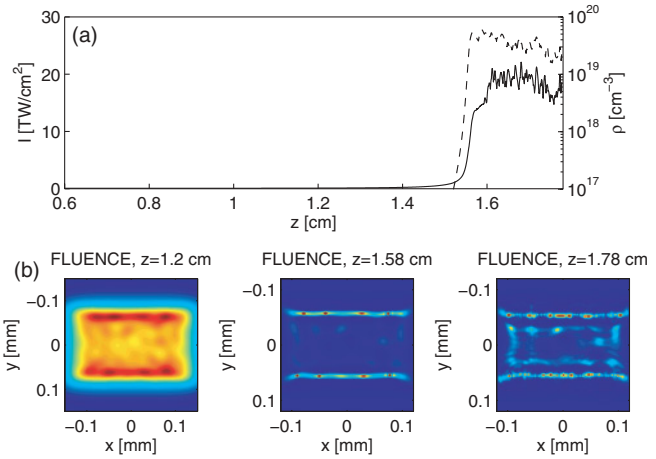

FIG. 3. (Color online) (a) Maximum intensity and peak electron density for the 355 nm pulse with long duration $t_p = 500$ fs and $w_0 = 200$ μm. (b) Fluence patterns $[\mathcal{F} \equiv \int I(t)dt]$ at different propagation distances.

In the above predictions we have mostly ignored perturbations inside the $(k_\perp, \overline{\omega})$ plane with $k_\perp \neq 0$ *and* $\overline{\omega} \neq 0$, even though they may have larger growth rates. The reason why those perturbations are not observed in the coming simulations is the following. Besides the linear growth of MI patterns, the beam also self-focuses as a whole, which leads to a continuous increase of the "background intensity" I_0 and makes the beam depart from an ideal plane-wave. The observed (numerical) MI patterns should thus be associated to a larger growth rate over an intensity range exceeding the usual validity domain $(|\mathcal{E}|^2 \lesssim 2I_0)$ of the classical MI theory. Thus, at fixed values of $k_\perp$ and $\overline{\omega}$ realizing $\Gamma_{\max}$, the growth rate must still be non zero for noticeable increase of the background intensity. We checked that this requirement was generally not fulfilled by data points belonging to the inner region of the $(k_\perp, \overline{\omega})$ plane. Some examples are illustrated in Fig. 2 [see blue, lower curve in Fig. 2(a)], displaying evidence of the predominance of the transverse instability over the temporal one. The same argument can moreover help us to predict which of the two temporal instabilities found in Fig. 1(c) may be the dominant one. As can be observed from Fig. 2(b), the growth rates using the lower frequency $\overline{\omega}_{\max} \simeq 0.15$ fs^{-1} (green, center line) clearly prevail over those computed from $\overline{\omega}_{\max} \simeq 0.52$ fs^{-1} (blue, lower line).

III. ULTRAVIOLET PULSES

We first focus on powerful beams propagating in normal dispersion regime. Starting from values less than 0.06 J/cm^2, the maximum beam fluence reaches ~2.5 J/cm^2 beyond the self-focusing distance of the 1 ps pulse and ~0.32 J/cm^2 for the 50 fs pulse. Since these fluences become close to the damage thresholds of dielectrics irradiated at low wavelengths [27,28], we restrict the self-channeling ranges to a few mm beyond the Kerr-focusing stage.

A. Long pulse durations (UV)

At the wavelength $\lambda_0 = 355$ nm, a "long" supergaussian pulse with $t_p = 500$ fs (FWHM $\simeq 1$ ps), small waist $w_0 = 200\,\mu$m, 100 critical powers, and suffering 5% random noise both in spatial and temporal amplitudes, develops regular modulations on its steepest boarders, before the most intense filaments reach the ionization threshold [29,30]. Figure 3(a) displays the evolution of the maximum pulse intensity and electron density. For clamping values $I_{\max} \simeq$ 15–20 TW/cm^2, the corresponding peak plasma density, $\rho_{\max} \simeq 4 \times 10^{19}$ cm^{-3}, agrees with Ref. [17]. In the stage preceding plasma generation, a ring pattern created from the supergaussian pulse [31] is amplified into a rectangular beam-shape upon propagation, as shown by the fluence patterns $[\mathcal{F} \equiv \int I(t)dt]$ of Fig. 3(b). About four small-scaled modulations emerge on each edge of the beam profile. These modulations appear regularly spaced by ~50 μm along the x-axis, where the beam shape is the more elongated. At $z = 1.2$ cm, the whole beam intensity has increased by 50% and collapse occurs 4 mm further. Beyond the nonlinear focus, the pulse decays into multiple filaments, first on the rectangular ring (~8 filaments), then inside the ring where the number of cells increases.

Figure 4 shows three surface plots of the pulse intensity profile in the (x, t) plane along the y coordinate supporting maximum intensity. In the x-direction, four modulations are clearly amplified before focus. Despite ~75 fs periodic undulations, no temporal oscillation seems amplified along z. Together with the transverse modulation length of ~46 μm ($\Gamma_{\max} \simeq 3.7$ cm^{-1}), these evaluations agree with the predictions made in Sec. II.

At the nonlinear focus ($z = 1.58$ cm), Fig. 4 shows that a dominant leading peak with about ~35 fs duration survives plasma defocusing, which damps components belonging to the rear pulse. The FWHM duration of the entire pulse, however, remains large, of the order of ~400 fs. Further on ($z >$ 1.7 cm), multiple filaments are nucleated due to the competition between Kerr and plasma nonlinearities in different pulse time slices [32]. Each resulting peak exhibits durations comprised between 10 fs and 50 fs. It is interesting to notice that the most spiky structures still occur at the leading and trailing edges of the pulse, suggesting thereby a collective action of the plasma response similar to the well-known scenario of "dynamic spatial replenishment" [33,34]. There is no particular optical shock formation owing to pulse

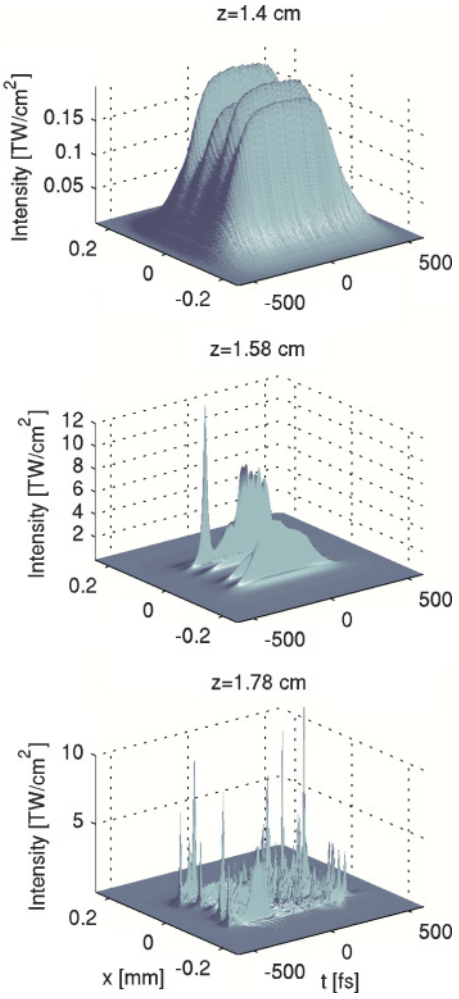

FIG. 4. (Color online) Field distributions of the long 355 nm pulse in the (x, t) plane at the coordinate (y) of maximum intensity ($y_{\max} \simeq -0.06$ mm) for three different propagation distances.

steepening effects, as the temporal gradient of the operator T is proportional to the laser wavelength and, thus, has a small influence at 355 nm [35].

In addition, we checked that the maximum intensity and peak electron density are in the expected order of magnitude. We indeed identified the intersection intensity between the photo-ionization rate $W(I)$ (assumed to prevail over avalanche ionization) and the ratio $(2\rho_c n_0 n_2/\Delta T \rho_{\rm nt}) \times I$ for a mean duration ΔT chosen as the temporal extent of the pulse shortened by the first ionization front. For the present pulse whose dominant peak is ~35 fs long at $z = 1.58$ cm, we obtain $I_{\max} = 19$ TW/cm^2 and $\rho_{\max} = 1.7 \times 10^{20}$ cm^{-3}, which are in reasonable agreement with Fig. 3(a).

B. Short pulse durations (UV)

We now examine the evolution of ultraviolet pulses having short duration ($t_p = 50$ fs) and broader waist ($w_0 = 1$ mm). The mean intensity is $I_0 \simeq 0.46$ TW/cm^2 at $z = 0$ and the pulse is initially perturbed by 5% random noise in amplitude only. Because such intensity level is reached by using a very large power ratio, $P_{\rm in}/P_{\rm cr} = 20\,000$, beam collapse occurs quite early, $z_c \simeq 2.45$ mm, as shown by Fig. 5(a). The fluence

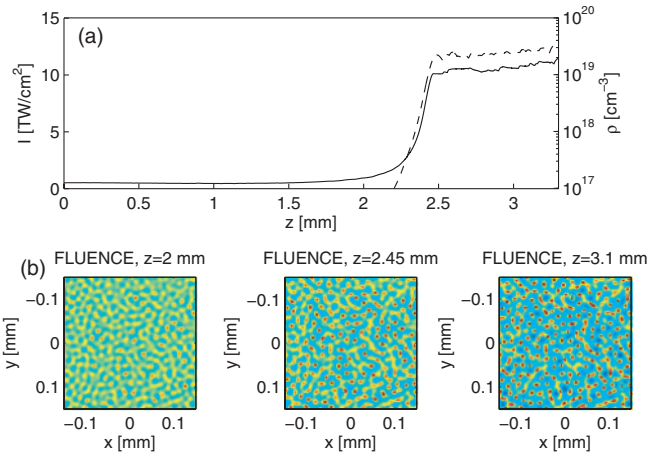

FIG. 5. (Color online) (a) Maximum intensity and peak electron density for the 355 nm pulse with short duration $t_p = 50$ fs and $w_0 = 1$ mm. (b) Fluence patterns detailing the filament growth at different propagation distances.

patterns displayed in Fig. 5(b) illustrate a multifilamentation regime taking place in the center of the beam, which is so intense that the supergaussian beam does not let its boarders amplify early modulations. In contrast to the previous case, the inner part of the beam serves as plane wave, subject to spatial modulations with periodic spacing of ~16 μm in the limit $\overline{\omega} \to 0$. This scale agrees with the modulations zoomed at $z = 2$ mm in Fig. 5(b). Further, the beam becomes highly turbulent in plasma regime ($z = 3.1$ mm), with interfilament distances of the order of 10 microns.

Figure 6 details (x, t) field distributions at specific propagation distances. Besides ~20 μm periodic striation along x, the pulse does not amplify temporal fluctuations during early propagation. Only spatial modulations grow. The corresponding wave number $k_\perp^{\max} \approx 3900$ cm^{-1} belongs to the instability region of maximum growth rate $\Gamma_{\max} \simeq 29.3$ cm^{-1}, as can be seen from Fig. 1(b). We can also notice the slight temporal broadening undergone by the pulse over 2 mm only, which we attribute to the strong GVD being more effective at short pulse durations. At focus, plasma generation acts in recompressing the pulse within a single hump of $\Delta T \sim 40$ fs duration only. Using this time interval and solving the expression

$$W(I) = \frac{2\rho_c n_0 n_2}{\Delta T \rho_{\rm nt}} \times I, \tag{10}$$

we estimate the clamping intensity and peak electron density to $I_{\max} \simeq 5.5$ TW/cm^2 and $\rho_{\max} = 5 \times 10^{19}$ cm^{-3}, which support the comparison with Fig. 5(a). Note that the peak electron density is slightly lower for short pulses. In this respect, analogous filamentation patterns created from weaker powers ($P_{\rm in} = 10\,000\, P_{\rm cr}$ with 1% spatial noise) were seen to develop peak densities limited to 6×10^{18} cm^{-3} only, after a more important temporal broadening occurs upon the first cm-long linear propagation stage (not shown here). Lowering the plasma response in dense media can be explained by the chromatic dispersion, which is reinforced at low wavelengths and short pulse durations [36,37].

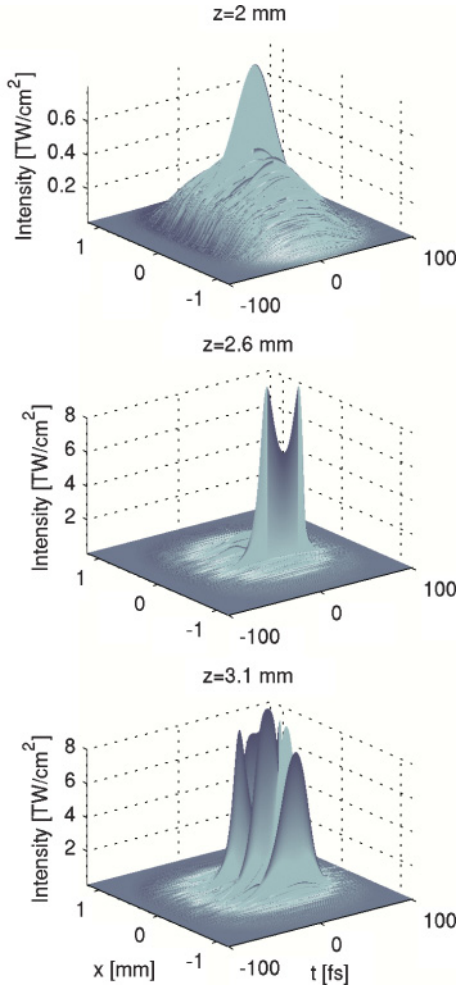

FIG. 6. (Color online) Field distributions of the short 355 nm pulse in the (x, t) plane at the coordinate y of maximum intensity for three propagation distances.

IV. INFRARED PULSES

Let us now examine characteristic pulse distortions for anomalous dispersion ($\lambda_0 = 1550$ nm). Starting from initial values $\leqslant 0.2$ J/cm^2, maximum beam fluence reaches 1.5–3 J/cm^2 and 0.43 J/cm^2 in plasma regime for long and short pulses, respectively. These values are close to damage thresholds reported at long wavelengths [28]. Therefore, propagation distances will again be limited to a few mm beyond the nonlinear focus.

A. Long pulse durations (IR)

We again start with long pulse durations ($t_p = 500$ fs) and small waist ($w_0 = 200$ μm) to emphasize potential breakup in time. Even with small powers, $P_{\rm in} = 10$ $P_{\rm cr}$, supergaussian beams are easily destabilized in space and undergo multiple filamentation on their ring profile [31]. With a mean input intensity of $I_0 \simeq 0.2$ TW/cm^2, the beam amplitude is perturbed both in space and time by a 5% random noise. Figure 7(a) shows in this respect that the beam intensity increases by 50% at $z = 1$ cm and beam collapse takes place at about $z_c \simeq 1.8$ cm. Figure 7(b) details fluence distributions at three characteristic distances around the nonlinear focus. From

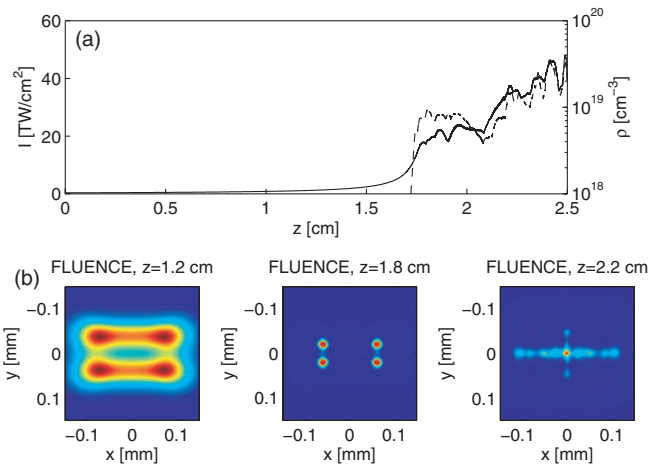

FIG. 7. (Color online) (a) Maximum intensity and peak electron density for the 1550 nm pulse with long duration $t_p = 500$ fs and $w_0 = 0.2$ mm. (b) Fluence patterns at different propagation distances.

$z = 0.8$ cm, four regular modulations arise with the transverse spacing of 120–150 μm upon the longest boarder in the x-direction (two modulations on each boarder). They amplify on the ridges of the ring ($z = 1.2$ cm), giving birth afterwards to four filaments ($z = 1.8$ cm). The most neighboring filaments then merge along the y-axis, before the resulting two cells coalesce in turn at center in full plasma regime ($z = 2.2$ cm). Other filaments can be nucleated at further distances, in the trace left by the primary ones [32].

Figure 8 illustrates the evolution of the (x, t) field distribution at maximum intensity along the y-axis for close propagation distances. Besides spatial instability, two sorts of temporal undulations appear: short-scaled ($\sim$10 fs) modulations that do not amplify and long-scaled ($\sim$50 fs) modulations that do amplify along the z-axis. These behaviors are compatible with Figs. 1(c) and 2(b). In space, the most unstable wave numbers nearby $k_\perp^{\rm max} \simeq 437$ cm^{-1}($\Gamma_{\rm max} \simeq 2$ cm^{-1}) correspond to 143 μm periodic modulations, which agrees with Fig. 7(b). At focus, plasma again defocuses every pulse component whose intensity is close to the clamping value. The front pulse then exhibits $\sim$40 fs FWHM duration. Note the persistent long/short modulations still surviving in the trailing edge of the pulse ($z = 1.8$ cm). At further distance ($z = 2.2$ cm), the pulse develops a full optically-turbulent regime. The strong refocusing in the rear pulse suggests an important action from the T, T^{-1} operators, reinforced at long wavelengths [35].

Using $\Delta T = 40$ fs and solving Eq. (10), we evaluated the clamping intensity and peak electron density to $I_{\rm max} \simeq 20$ TW/cm^2 and $\rho_{\rm max} = 6 \times 10^{18}$ cm^{-3}, which agrees with Fig. 7(a).

B. Short pulse durations (IR)

The last configuration concerns the multifilamentation of ultrashort ($t_p = 50$ fs) pulses with millimeter waist ($w_0 = 1$ mm) and anomalous dispersion ($\lambda_0 = 1550$ nm). Only the spatial amplitude of the beam is perturbed by a 5% random noise, altering the initial intensity level $I_0 \simeq 0.73$ TW/cm^2

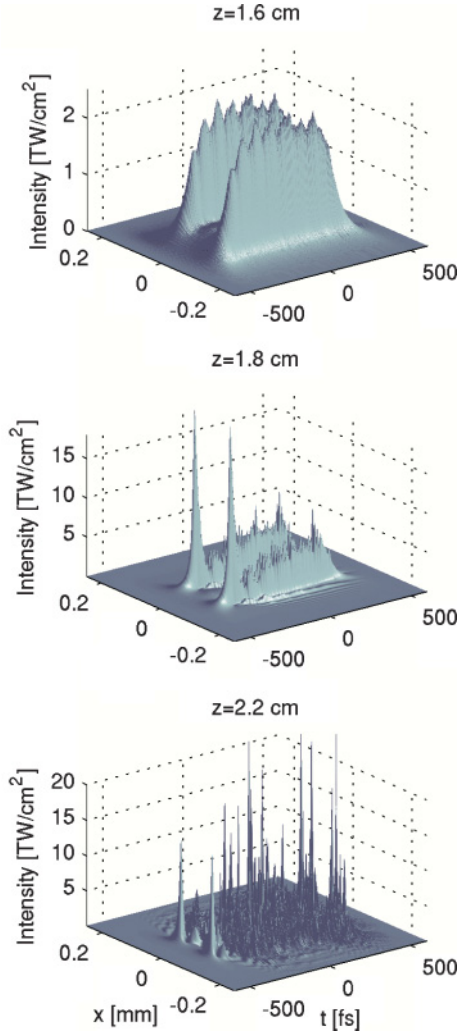

FIG. 8. (Color online) Field distributions of the long 1550 nm pulse in the (x, t) plane at the respective coordinates y of maximum intensity (from top to bottom: $y_{max} \simeq 0.028$, 0.019, and 0 mm) and for three propagation distances.

reached for $P_{in} = 1000\, P_{cr}$ in silica. For this purpose, Fig. 9(a) displays the global evolution of the beam, which collapses at the self-focusing distance $z \simeq 0.8$ cm. At such high power levels, there is no spatial breakup occurring on the ring pattern. Instead, the central zone of the beam becomes rapidly turbulent and self-organizes into myriads of cells distributed into bee-nested structures. These structures are characterized by micrometric hot zones, in which filaments are nucleated and connected to each other by high-fluence bridges [see Fig. 9(b)]. Before the focus, spatial modulations are amplified from the periodic spacing $\lambda_{opt} \simeq 70\ \mu$m ($z = 6$ mm). This evaluation fully agrees with the maximum wave number of Fig. 1(d).

Along the time direction, Fig. 1(d) predicts the occurrence of temporal modulations with ~18 fs period. Such modulations, which are not initially excited, are absent from our numerical simulations. As a matter of fact, anomalous dispersion and steepening effects, prominent at short pulse durations, push and compress all spatial components toward the back zone of the pulse [38]. This not only breaks the plane-wave assumption for modulational instability in time,

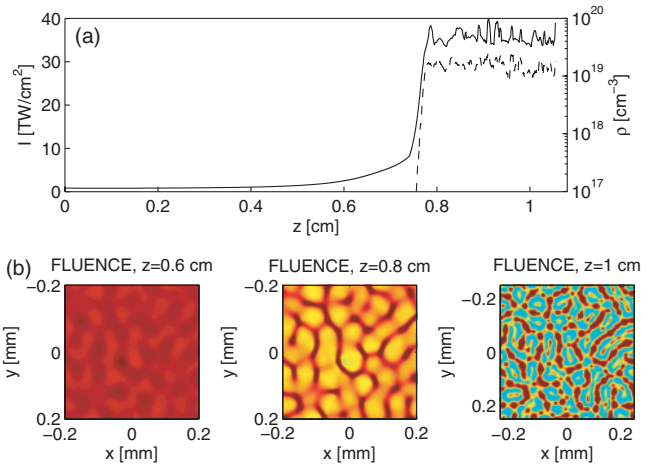

FIG. 9. (Color online) (a) Maximum intensity and peak electron density for the 1550 nm pulse with short duration $t_p = 50$ fs and $w_0 = 1$ mm. (b) Fluence patterns at different propagation distances.

but also inhibits the classical stage of plasma-driven pulse splitting in time. These effects superimpose for compressing the pulse down to two optical cycles (~10 fs at focus) and they further initiate a strong shock dynamics along which singly-cycled (~5 fs) spikes can dominate, as can be seen in Fig. 10. It is interesting to notice the important number of filaments regularly formed along the x-axis; each generates one cell displayed in Fig. 9(b). Along the full self-channeling range ($z \geqslant 0.9$ cm), the pulse temporal centroid goes on moving toward positive times due to third-order dispersion and pulse steepening. Using the evaluation $\Delta T = 5$–10 fs for the most intense peak formed at focus, we estimate from Eq. (10) $I_{max} = 26$–30 TW/cm^2 and $\rho_{max} = 7.6$–8.8×10^{18} cm^{-3}, which is again compatible with Fig. 9(a).

To end this subsection, we find it instructive to prove from multifilamented short pulses that the spatial landscape may drastically change from one time slice to another. At the time slice supporting the maximum intensity ($t = t_{max}$), the beam blows up into multiple filaments at center, unlike what could be expected for a supergaussian beam forming a ring pattern at moderate input intensities. Around t_{max} filaments emerge, dissipate due to plasma losses, and renucleate inside the most intense central part of the beam. In contrast, other time slices, i.e., at $t = 0$, can convey in the leading part of the pulse different spatial landscapes, e.g., the expected ring patterns, that survive at lower intensity levels. Here, plasma generation is negligible and, due to its large waist ($w_x \simeq 1.2$ mm, $w_y \simeq 0.75$ mm), the ring slowly diffracts in linear propagation regime (see Fig. 11).

V. SPECTRA

Finally, we comment on the spectral modifications undergone by the different pulses. Figure 12 displays the intensity spectra averaged over the entire simulation box at $z = 0$ (dotted curves) and at the three propagation distances selected in the previous (x, t) field distributions. Plotstyle follows the three increasing distances shown in Figs. 4, 6, 8, and 10, represented by dash, dash-dotted, and solid curves, respectively.

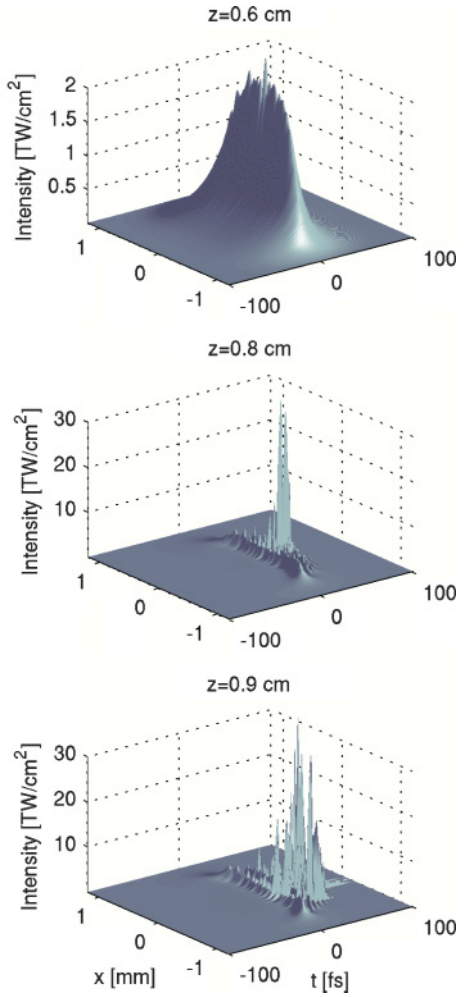

FIG. 10. (Color online) Field distributions of the short 1550 nm pulse in the (x, t) plane at the coordinate y of maximum intensity and for three propagation distances.

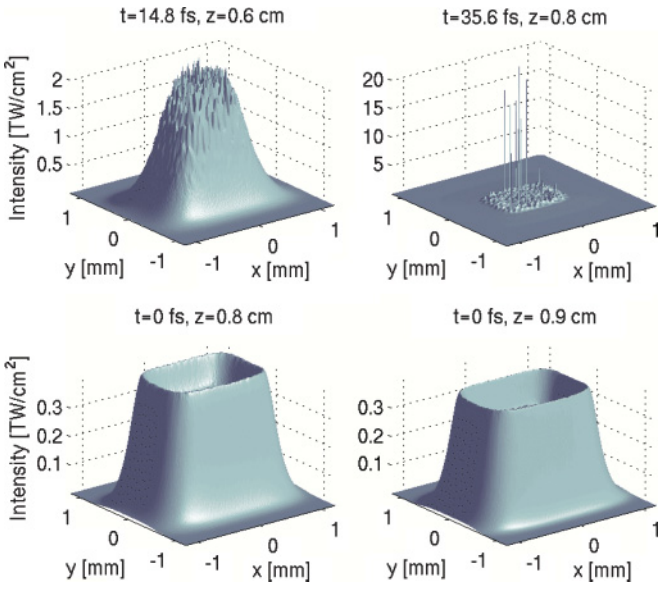

FIG. 11. (Color online) Maximum intensity profiles in the diffraction plane (top) at times $t = t_{max}$ and (bottom) at $t = 0$, for propagation distances around the self-focus point.

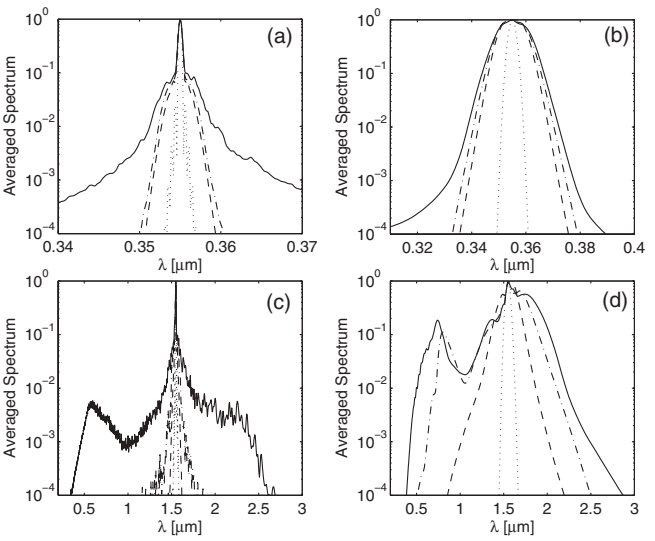

FIG. 12. Averaged spectra for (a) 355 nm long pulses, (b) 355 nm short pulses, (c) 1550 nm long pulses, and (d) 1550 nm short pulses. Plotstyles are explained in the text.

Figures 12(a) and 12(b) both indicate a narrow spectral broadening, which remains almost symmetric even during the self-channeling stage. We can also observe that the spectra remain unchanged in their first intensity decade. This small spectral broadening can be justified by the fact that supercontinuum generation is generally limited in the UV and the operators T, T^{-1}, asymmetrizing the spectral shape, have a negligible influence at low wavelengths [35]. Self-phase modulation, dictated by the frequency variations $\Delta\omega \sim -k_0 \Delta z (n_2 I_{max} - \rho_{max}/2n_0\rho_c)/\tau_{FWHM}$ along path intervals Δz and pulse durations τ_{FWHM}, thus appears limited, first because the intensity is moderately clamped at levels <20 TW/cm^2, second because the overall FWHM pulse duration always stays comparable with the initial one ($\tau_{FWHM} \sim t_p$).

In contrast, Figs. 12(c) and 12(d) reflect the fact that both short and long 1550 nm pulses undergo sharp intensity growths ($I_{max} > 30$ TW/cm^2), accompanied by strong temporal compression dynamics. The latter is reinforced by optical shocks induced by an efficient self-steepening. Consequently, the pulse spectrum widely broadens to large frequencies, as already reported, e.g., at infrared wavelengths in air [39] or at 1550 nm in silica for a single filament [40].

Another interesting feature is the growing lateral spectral components that surround the central frequency. Their dynamics could resemble those reported recently on rogue wave formation in 1D (optical fiber) systems at long wavelengths [41]. Despite the lack of numerous simulations testing different noise realizations, we can guess that optical rogue waves, characterized by the sudden occurrence of intense components shifted to the back zone, may also here appear around the self-focus point. In this regards, we can be inspired by the temporal distribution of spikes for long pulses in Fig. 8 and by the "rogue" trailing pulse amplified from initially short pulses in Fig. 10. Optical rogue waves were recently reported in atmospheric laser filamentation from the statistical analysis of experimental spectra [42].

VI. CONCLUSION

In summary, we have numerically examined the self-focusing and multiple filamentation of pulses at two different wavelengths inducing normal or anomalous group-velocity dispersion. The analysis was performed for small (micrometer) spatial beams limiting the creation of small-scaled cells, but extending over long pulse durations, and for large (millimeter) beams triggering a very large number of filaments over relatively short time scales. In this respect, an important result is the applicability of the spatial light replenishment scenario creating two-peaked temporal profiles on multifilamented beams not only in the UV, but also in the near-infrared domain over long pulses. Here the plasma classically acts in collective manner to defocus the trailing edge of the most intense spatial components and reform secondary peaks in the same zone at further distances. Long pulse durations diminish the efficiency of anomalous dispersion in the near-infrared domain. In contrast, the same effect becomes a key player for initially-short pulse durations. Combined with higher-order dispersion and steepening effects, it leads to pulse self-compression in the rear region. There, multiple filaments can emerge in space, whereas at earlier times more regular patterns, such as ring distributions, still survive over long z scales. For ultraviolet pulses, we find moderate changes in the temporal extent, associated with a small spectral broadening that still holds in multifilamentation regime. Finally, we checked by means of arguments based on the modulational instability theory that characteristic fluctuations amplified by the Kerr nonlinearities could be found in such beams.

ACKNOWLEDGMENTS

This work was granted access to the HPC resources of CCRT under the allocation 2009-x2009106003 made by GENCI (Grand Equipement National de Calcul Intensif). It was also supported through the "Grand Challenge/Titane" program of the CEA. In this respect, the authors thank Laurent Nguyen for his precious help in the exploitation of the cluster Titane.

[1] S. L. Chin, S. A. Hosseini, W. Liu, Q. Luo, F. Théberge, N. Aközbek, A. Becker, V. P. Kandidov, O. G. Kosareva, and H. Schroeder, Can. J. Phys. **83**, 863 (2005).
[2] A. Couairon and A. Mysyrowicz, Phys. Rep. **441**, 47 (2007).
[3] L. Bergé, S. Skupin, R. Nuter, J. Kasparian, and J. P. Wolf, Rep. Prog. Phys. **70**, 1633 (2007).
[4] J. Kasparian and J.-P. Wolf, Opt. Express **16**, 466 (2008).
[5] V. P. Kandidov, S. A. Shlenov, and O. G. Kosareva, Quant. Electron. **39**, 205 (2009).
[6] A. Zaïr, A. Guandalini, F. Schapper, M. Holler, J. Biegert, L. Gallmann, A. Couairon, M. Franco, A. Mysyrowicz, and U. Keller, Opt. Express **15**, 5394 (2007).
[7] S. Skupin, G. Stibenz, L. Bergé, F. Lederer, T. Sokollik, M. Schnürer, N. Zhavoronkov, and G. Steinmeyer, Phys. Rev. E **74**, 056604 (2006).
[8] X. Chen, Y. Leng, J. Liu, Y. Zhu, R. Li, and Z. Xu, Opt. Commun. **259**, 331 (2006).
[9] V. I. Bespalov and V. I. Talanov, JETP Lett. **3**, 307 (1966).
[10] A. J. Campillo, S. L. Shapiro, and B. R. Suydam, Appl. Phys. Lett. **24**, 178 (1974).
[11] L. Bergé, S. Skupin, F. Lederer, G. Méjean, J. Yu, J. Kasparian, E. Salmon, J. P. Wolf, M. Rodriguez, L. Wöste *et al.*, Phys. Rev. Lett. **92**, 225002 (2004).
[12] A. Dubietis, G. Tamošauskas, G. Fibich, and B. Ilan, Opt. Lett. **29**, 1126 (2004).
[13] G. Méchain, A. Couairon, M. Franco, B. Prade, and A. Mysyrowicz, Phys. Rev. Lett. **93**, 035003 (2004).
[14] V. P. Kandidov, N. Aközbek, M. Scalora, O. G. Kosareva, A. V. Nyakk, Q. Luo, S. A. Hosseini, and S. L. Chin, Appl. Phys. B: Lasers & Optics **80**, 267 (2005).
[15] S. Tzortzakis, L. Sudrie, M. Franco, B. Prade, A. Mysyrowicz, A. Couairon, and L. Bergé, Phys. Rev. Lett. **87**, 213902 (2001).
[16] L. Sudrie, A. Couairon, M. Franco, B. Lamouroux, B. Prade, S. Tzortzakis, and A. Mysyrowicz, Phys. Rev. Lett. **89**, 186601 (2002).
[17] D. G. Papazoglou, I. Zergioti, and S. Tzortzakis, Opt. Lett. **32**, 2055 (2007).
[18] L. Sudrie, M. Franco, B. Prade, and A. Mysyrowicz, Opt. Commun. **171**, 279 (1999).
[19] T. Tamaki, W. Watanabe, H. Nagai, M. Yoshida, J. Nishii, and K. Itoh, Opt. Express **14**, 6971 (2006).
[20] G. P. Agrawal, *Nonlinear Fiber Optics*, 3rd ed. (Academic Press, San Diego, 2001).
[21] T. Brabec and F. Krausz, Phys. Rev. Lett. **78**, 3282 (1997).
[22] A. A. Zozulya, S. A. Diddams, A. G. Van Engen, and T. S. Clement, Phys. Rev. Lett. **82**, 1430 (1999).
[23] L. V. Keldysh, Sov. Phys. JETP **20**, 1307 (1965).
[24] D. Milam, Appl. Opt. **37**, 546 (1998).
[25] K. Rypdal and J. J. Rasmussen, Phys. Scr. **40**, 192 (1989).
[26] A. G. Litvak, T. A. Petrova, A. M. Sergeev, and A. D. Yunakovskii, Sov. J. Plasma Phys. **9**, 287 (1983).
[27] S. Tamura, S. Kimura, Y. Sato, S. Motokoshi, H. Yoshida, and K. Yoshida, Jpn. J. Appl. Phys. **29**, 1960 (1990).
[28] B. C. Stuart, M. D. Feit, S. Herman, A. M. Rubenchik, B. W. Shore, and M. D. Perry, Phys. Rev. B **53**, 1749 (1996).
[29] L. Guyon, F. Courvoisier, V. Boutou, R. Nuter, A. Vinçotte, S. Champeaux, L. Bergé, P. Glorieux, and J.-P. Wolf, Phys. Rev. A **73**, 051802(R) (2006).
[30] A. Vinçotte and L. Bergé, Physica D (Amsterdam) **223**, 163 (2006).
[31] L. Bergé, C. Gouédard, J. Schjødt-Eriksen, and H. Ward, Physica D (Amsterdam) **176**, 181 (2003).
[32] S. A. Hosseini, Q. Luo, B. Ferland, W. Liu, S. L. Chin, O. G. Kosareva, N. A. Panov, N. Aközbek, and V. P. Kandidov, Phys. Rev. A **70**, 033802 (2004).
[33] M. Mlejnek, E. M. Wright, and J. V. Moloney, Opt. Lett. **23**, 382 (1998).
[34] M. Mlejnek, M. Kolesik, J. V. Moloney, and E. M. Wright, Phys. Rev. Lett. **83**, 2938 (1999).

[35] S. Skupin and L. Bergé, Opt. Commun. **280**, 173 (2007).
[36] M. Kolesik, E. M. Wright, and J. V. Moloney, Phys. Rev. Lett. **92**, 253901 (2004).
[37] S. Skupin, R. Nuter, and L. Bergé, Phys. Rev. A **74**, 043813 (2006).
[38] L. Bergé and S. Skupin, Phys. Rev. E **71**, 065601(R) (2005).
[39] N. Aközbek, M. Scalora, C. M. Bowden, and S. L. Chin, Opt. Commun. **191**, 353 (2001).
[40] S. Skupin and L. Bergé, Physica D (Amsterdam) **220**, 14 (2006).
[41] J. M. Dudley, G. Genty, and B. J. Eggleton, Opt. Express **16**, 3644 (2008).
[42] J. Kasparian, P. Béjot, J.-P. Wolf, and J. M. Dudley, Opt. Express **17**, 12070 (2009).